

Exploring parity magnetic effects through quantum simulation with superconducting qubits

Yu Zhang,^{1,2,§} Yan-Qing Zhu^{3,§} Jianwen Xu,^{1,2,§} Wen Zheng^{1,2,*} Dong Lan^{1,2,4}
 Giandomenico Palumbo⁵, Nathan Goldman,⁶ Shi-Liang Zhu^{7,8} Xinsheng Tan^{1,2,4,†}
 Z.D. Wang,^{3,‡} and Yang Yu^{1,2,4}

¹*National Laboratory of Solid State Microstructures, School of Physics, Nanjing University, Nanjing 210093, China*

²*Shishan Laboratory, Suzhou Campus of Nanjing University, Suzhou 215000, China*

³*Guangdong-Hong Kong Joint Laboratory of Quantum Matter, Department of Physics, and HK Institute of Quantum Science & Technology, The University of Hong Kong, Pokfulam Road, Hong Kong, China*

⁴*Hefei National Laboratory, Hefei 230088, China*

⁵*School of Theoretical Physics, Dublin Institute for Advanced Studies, 10 Burlington Road, Dublin 4, Ireland*

⁶*Center for Nonlinear Phenomena and Complex Systems, Université Libre de Bruxelles, CP 231, Campus Plaine, Brussels B-1050, Belgium*

⁷*Key Laboratory of Atomic and Subatomic Structure and Quantum Control (Ministry of Education), School of Physics, South China Normal University, Guangzhou 510006, China*

⁸*Guangdong Provincial Key Laboratory of Quantum Engineering and Quantum Materials, Guangdong-Hong Kong Joint Laboratory of Quantum Matter, South China Normal University, Guangzhou 510006, China*



(Received 19 August 2023; revised 20 February 2024; accepted 23 February 2024; published 25 March 2024)

We present a successful realization of four-dimensional semimetal bands featuring tensor monopoles, achieved using superconducting quantum circuits. Our experiment involves the creation of a highly tunable diamond energy diagram with four coupled transmons, and the parametric modulation of their tunable couplers, effectively mapping momentum space to parameter space. This approach enables us to establish a four-dimensional Dirac-like Hamiltonian with fourfold degenerate points. Moreover, we manipulate the energy of tensor monopoles by introducing an additional pump microwave field, generating effective magnetic and pseudoelectric fields and simulating topological parity magnetic effects emerging from the parity anomaly. Utilizing nonadiabatic response methods, we measure the fractional second Chern number for a Dirac valley with a varying mass term, signifying a nontrivial topological phase transition connected to a five-dimensional Yang monopole. Our work lays the foundation for further investigations into higher-dimensional topological states of matter and enriches our comprehension of topological phenomena.

DOI: 10.1103/PhysRevApplied.21.034052

I. INTRODUCTION

Topological phases of matter have attracted broad interest from different physical communities ranging from condensed matter [1–3] to synthetic systems [4–9], being at the heart of modern physics. One of the intriguing and exciting features is that these novel phases support topological electromagnetic responses described by the associated topological field theory [10,11]. For instance, in the well-known three-dimensional (3D) Weyl semimetals, the chiral magnetic effect is induced by a paired Weyl dipole resulting from the chiral anomaly [12–16].

In two-dimensional (2D) dipolar Dirac semimetals, parity anomaly induces the pseudo-Hall effect [17] with the pseudoelectric field arising from an external strain field [18–20]. Additionally, significant attention has also been given to the quantum anomalous Hall effect in 2D Chern insulators and the topological magnetoelectric effect in 3D topological insulators [21].

By contrast, topological phases and the related electromagnetic effects in higher dimensions are much less studied, especially in experiments. This is primarily due to the constraint of natural materials that can be used in such experiments. Fortunately, quantum simulations using synthetic matter have emerged as a powerful tool for simulating higher-dimensional topological states of matter, owing to their high flexibility and controllability. For instance, the four-dimensional (4D) quantum Hall physics [21–24] and the corresponding Thouless pumping

*zhengwen@nju.edu.cn

†tanxs@nju.edu.cn

‡zhang@hku.hk

§These authors contributed equally to this work.

in 2D [25] have been experimentally realized in ultracold atoms [26,27] and photonics [28]. Recently, a distinct kind of 4D tensor monopole, characterized by the first Dixmier-Douady (\mathcal{DD}) invariant, has been theoretically investigated [29–33] and experimentally realized in superconducting circuits [34] and nitrogen-vacancy (N-V) centers [35]. In addition, the parity magnetic effect (PME) arising from the parity anomaly in 4+1 dimensions induced by a pair of 4D monopoles has been predicted in a 4D topological semimetal [31]. However, no experimental demonstration has been reported about this novel topological electromagnetic effect so far.

II. RESULTS

In this paper, we emulate a 4D topological semimetal band with tensor monopoles by using superconducting quantum circuits. We show how to detect the PME in this system by generating an effective magnetic (pseudoelectric) field and measuring the second Chern number (SCN) of a massive Dirac-like cone after introducing a mass regulator for a 4D monopole. Interestingly, the corresponding gapped system with two Dirac-like valleys hosts opposite fractional SCN, which exhibits a so-called valley-induced magnetic effect similar to the gapless case. Meanwhile, this gapped system can be characterized by a second valley Chern number defined as a half difference of the SCN for two valleys, and its behavior follows the 4D valley Hall effect predicted in the recent work [36]. Similar methods in our superconducting system can also detect this second valley Chern number and valley Hall effect. We also present a discussion about the topological phase transition based on this 4D model.

A. Experimental setup

The layout of our device is shown in Fig. 1, where four transmon qubits form a 2×2 square lattice [37–41]. Each side of the square consists of two transmons connected to a center tunable coupler with the same coupling strength and further coupled to each other directly through a residue capacitance. Each qubit and coupler is labeled as Q_i and C_j , respectively, where $i, j \in \{1, 2, 3, 4\}$. The system quantum crosstalk has been analyzed recently in this kind of multiqubit lattice [42–44]. Considering the nearest-neighbor coupling, the entire Hamiltonian of the system can be written as

$$\frac{H}{\hbar} = \sum_{i,j=1}^4 \left[-\frac{1}{2}\omega_{Q_i}\sigma_{Q_i}^z - \frac{1}{2}\omega_{C_j}(\phi_j)\sigma_{C_j}^z + (g_{ij}\sigma_{Q_i}^+\sigma_{C_j}^- + g_{i+1,j}\sigma_{Q_{i+1}}^+\sigma_{C_j}^- + \text{h.c.}) \right], \quad (1)$$

where the qubit frequencies ω_{Q_i} are designed negatively detuned from the nearest coupler ω_{C_j} , $\Delta_{ij} = \omega_{Q_i} - \omega_{C_j} < 0$.

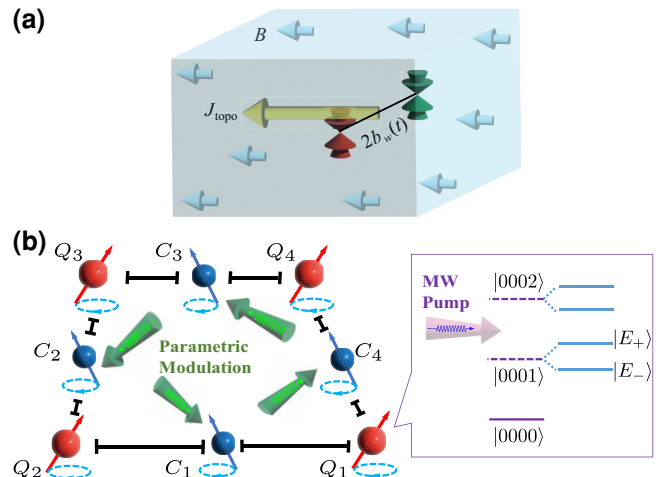


FIG. 1. (a) Schematic of parity magnetic effect. A pair of 4D monopoles exist in momentum space. The separation $b_w(t)$ is modulated artificially to create an effective electric field $E_5^w = \partial_t b_w$. In the presence of a static magnetic field B , a topological current J_{topo} will be induced. (b) The device consists of four transmons (red) and four couplers (blue). Four parametric modulations with different frequencies generate the Hamiltonian (green arrows), while an additional pump signal is applied to Q_1 to simulate the fictitious chemical potential. The lower energy level $|E_-\rangle$ and the first excited states of other qubits constitute the adjustable first excited manifold.

The coupling between qubit and coupler $g_{ij} \ll |\Delta_{ij}|$, meaning that the couplers can be adiabatically eliminated. Therefore, we obtain the effective coupling strength $J_{i,i+1}$ between adjacent qubits [45–47].

In this approach, we use parametric modulation to realize the designed Hamiltonian. We apply four independent sinusoidal fast-flux biases $\phi_j(t) = \Phi_j + \delta_j \cos(\omega_{\phi_j} t + \varphi_j)$ to coupler C_j , respectively, and obtain resonant exchange interaction $\Omega_{i,i+1} = (\delta_j/2)(\partial J_{i,i+1}/\partial \phi_j)e^{-i\varphi_j}$ [48–53]. In the subspace spanned by $\{|1000\rangle, |0100\rangle, |0010\rangle$, and $|0001\rangle\}$ (the order of Q_1 and Q_2 is exchanged here), the Hamiltonian can be written as

$$\frac{H_{\text{eff}}}{\hbar} = \begin{bmatrix} 0 & \Omega_{12}^* & \Omega_{23} & 0 \\ \Omega_{12} & 0 & 0 & \Omega_{41}^* \\ \Omega_{23}^* & 0 & 0 & \Omega_{34} \\ 0 & \Omega_{41} & \Omega_{34}^* & 0 \end{bmatrix}, \quad (2)$$

showing a diamond configuration. Here the coupling strengths and phases are tunable, and both can be easily calibrated.

B. Topological model and response

By mapping the system parameters into the Bloch vectors, i.e., $\Omega_{12} = d_x + ad_w + i(d_z + ad_y)$, $\Omega_{23} = d_w + ad_x - i(d_y + ad_z)$, $\Omega_{34} = d_x - ad_w + i(-d_z + ad_y)$, and $\Omega_{41} = -d_w + ad_x + i(-d_y + ad_z)$, we demonstrate that

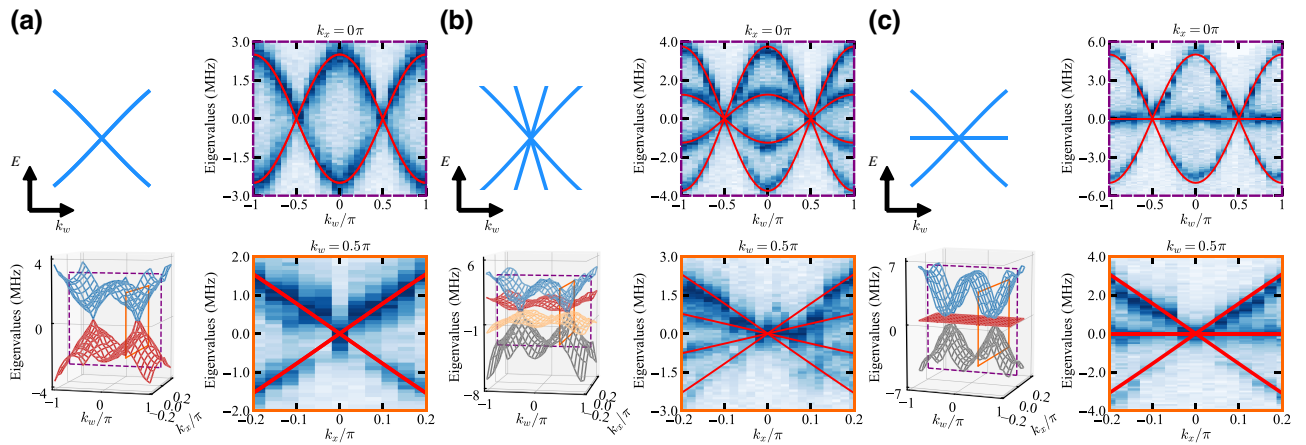


FIG. 2. Difference spectra $E(k_w)$ in the FBZ for $a = 0, 0.5$, and 1 in (a)–(c), respectively. The upper left panels are the schematic energy dispersion $E(k_w)$ at $k_{x,y,z} = 0$ near the right nodal point. The lower left panels demonstrate the measured energy spectrum of 4D topological semimetals by changing k_w and k_x . The purple dashed frame and the orange solid frame mark the cross sections corresponding to the data in the right panels. The 1D spectra are shown in the upper and lower right panels. The theoretical calculation (red lines) agrees well with the experimental results.

our diamond-type coupling can be used to simulate the momentum-space Hamiltonian [31] as

$$H(\mathbf{k}) = d_x \tilde{\Gamma}_x + d_y \tilde{\Gamma}_y + d_z \tilde{\Gamma}_z + d_w \tilde{\Gamma}_w, \quad (3)$$

with the four-component Bloch vector $d_i = v_i \sin k_i$ for $i \in \{x, y, z\}$, and $d_w = v_w (\Lambda + 3 - \sum_{j=x,y,z,w} \cos k_j)$. Here v_i denotes the Fermi velocity, and Λ is a tunable parameter. The matrices are $\tilde{\Gamma}_x = \sigma_0 \otimes \sigma_1 + a \sigma_1 \otimes \sigma_0$, $\tilde{\Gamma}_y = \sigma_2 \otimes \sigma_3 + a \sigma_3 \otimes \sigma_2$, $\tilde{\Gamma}_z = \sigma_0 \otimes \sigma_2 + a \sigma_2 \otimes \sigma_0$, and $\tilde{\Gamma}_w = \sigma_1 \otimes \sigma_3 + a \sigma_3 \otimes \sigma_1$, where a is constant, σ_k are the standard Pauli matrices, and σ_0 is the identity matrix.

Note that this model always preserves chiral symmetry, i.e., $\{\mathcal{S}, H\} = 0$ with $\mathcal{S} = \tilde{\Gamma}_0 = \sigma_3 \otimes \sigma_3$. The energy spectrum of this model is given by $E = \pm(1 \pm a)\sqrt{\sum_j d_j^2}$. For $\Lambda < |1|$, the system hosts two monopoles near $\mathbf{K}_{\pm} = (0, 0, 0, \pm \arccos \Lambda)$ with the effective Hamiltonian

$$H_{\pm}(\mathbf{q}^{\pm}) = q_x^{\pm} \tilde{\Gamma}_x + q_y^{\pm} \tilde{\Gamma}_y + q_z^{\pm} \tilde{\Gamma}_z \pm \beta q_w^{\pm} \tilde{\Gamma}_w, \quad (4)$$

where $\beta = \sqrt{1 - \Lambda^2}$ and $\mathbf{q}^{\pm} = \mathbf{k} - \mathbf{K}_{\pm}$. There are two types of monopoles for H_{\pm} when a takes different values. For $a = 0$, it is a \mathbb{Z}_2 monopole characterized by a 3D winding number $w = 1$ and is protected by an additional symmetry \mathcal{CP} involving charge conjugation (\mathcal{C}) and inversion (\mathcal{P}), i.e., $\{\mathcal{CP}, H\} = 0$ with $\mathcal{CP} = \sigma_1 \otimes \sigma_2 \mathcal{K}$ satisfying $(\mathcal{CP})^2 = -1$. For $a \neq 0$, H_{\pm} breaks \mathcal{CP} but only keeps chiral symmetries, which is coined tensor monopoles characterized by the \mathcal{DD} invariant belonging to \mathbb{Z} class [29,30]. Notably, a tensor monopole H_{\pm} hosts the topological charge $\mathcal{DD} = \pm 2$ for $a \neq 0, \pm 1$ while $\mathcal{DD} = \pm 1$ for $a = \pm 1$ due to the flat limit. All the above topological numbers are defined on the 3D hypersphere enclosing the monopole. Thus it implies this system presents

a monopole-to-monopole topological phase transition by tuning the parameter a [31].

To experimentally visualize the band configuration of this 4D topological semimetal, we measure the spectra of the Hamiltonian $H(\mathbf{k})$ in the first Brillouin zone (FBZ). As shown in Fig. 2(a), we measure two twofold-degenerate energy bands with a pair of \mathbb{Z}_2 monopoles for the spin-1/2 case when $a = 0$. As we increase parameter a to be $0 < |a| < 1$, the degeneracy for each monopole is lifted, which gives a tensor semimetal phase with four energy bands as shown in Fig. 2(b) with $a = 0.5$. Especially when $a = \pm 1$, two middle bands become perfectly flat, so we can only observe three energy levels near the tensor monopoles, as illustrated in Fig. 2(c). In Figs. 2(a)–2(c), we set $\Lambda = 0$ for simplicity. Additionally, we can vary the parameter Λ without difficulty, tuning the separation between two monopoles.

For such a 4D semimetal phase with a pair of monopoles with opposite charges separated along the k_w direction with the distance $|\mathbf{K}_+ - \mathbf{K}_-| = 2b_w$, an anomalous topological current will be generated in the presence of a magnetic field $\mathbf{B} = B^z \hat{e}_z$ and a pseudoelectric field $E_5^w = \partial_t b_w$ [14,19,20,54], which is given by [31]

$$J^z = \frac{C_2^+}{2\pi^2} E_5^w B^z. \quad (5)$$

Note that C_2^+ is the SCN for a single Dirac-like valley near \mathbf{K}_+ described by $H_{v,+} = H_+ + \tilde{m}$ when performing the Pauli-Villars method by introducing a chiral-broken mass regulator $\tilde{m} = m \tilde{\Gamma}_0$ to open the gap. One has $C_2^+ = \text{sgn}(m)/2$ for $a \neq \pm 1$ while $C_2^+ = \text{sgn}(m)/8$ for $a = \pm 1$. Namely, the topological current induced by two tensor monopoles in the flat limit is only 1/4 of those cases

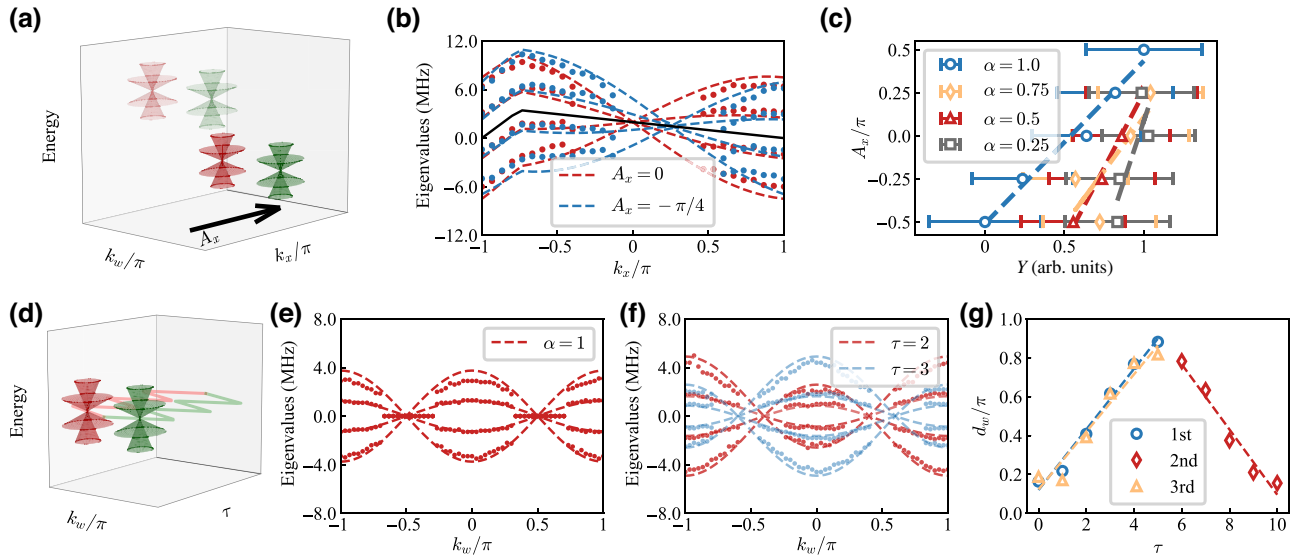


FIG. 3. Experimental results for $a = 0.5$. (a) Diagram of the effects of A_x used to apply effective magnetic field. (b) Spectrum along the k_x direction for $u_0(\mathbf{k}) = f(k_x)$ (black line). The vector potential A_x is set to 0 and $-\pi/4$, respectively. The dashed lines are the theoretical results, and the dots are the extracted experimental data. (c) Plot showing how A_x varies with Y for different α , extracting different magnetic fields. (d) Illustration of the modulation of the monopole separation under a static magnetic field. (e) Spectrum along the k_w axis without modulation ($\Lambda = 0$) under a static magnetic field. (f) Spectrum at different discrete times τ under a time-dependent modulation $\Lambda(\tau)$ for $\tau = 2$ (red) and $\tau = 3$ (blue) with $\alpha = 1.0$. (g) The monopole separation changes in different magnetic fields with fictitious time. For $\alpha = 1.0$, τ changes from 0 to 5 (blue) and from 6 to 10 (red), and for $\alpha = 0.5$, τ changes from 0 to 5 (yellow).

for $a \neq \pm 1$. Similarly, another valley near \mathbf{K}_- described by $H_{v,-} = H_- + \tilde{m}$ hosts an opposite SCN, i.e., $C_{2,-} = -C_{2,+}$, in contrast to $H_{v,+}$.

PME in the semimetal phase ($m = 0$) without a gap shares the same results as its corresponding gapped system ($m \neq 0$) when we effectively introduce a chiral-broken mass term \tilde{m} into $H(\mathbf{k})$. The topological response is also named “valley-induced magnetic effect,” which has been well studied in Ref. [36] recently. The total system $H_{\text{tot}} = H + \tilde{m}$ can now be characterized by the second valley Chern number $C_{2,v} = (C_2^+ - C_2^-)/2 = C_2^+$. Therefore, this system also supports the so-called “4D quantum valley Hall effect” when subjected to both an electric field (E^z) and a magnetic field (B^z), resulting in a valley current as $J_5^z = (C_{2,v}/4\pi^2)E^zB^z$, where two valleys contribute opposite Hall currents [36].

In the following, we show how to emulate this PME in our superconducting system. In order to generate a magnetic field, we introduce a momentum-dependent energy shift $u_0(\mathbf{k})$, $H_{\text{pump}}/\hbar = H_{\text{eff}}/\hbar + u_0(\mathbf{k})I_4$, with I_4 being a 4×4 identity matrix. We utilize the Autler-Townes splitting to manipulate the energy shift [55–59]. Specifically, we apply an extra pump microwave field $\Omega_d \cos(\omega_d t + \varphi_d)(\sigma_{Q_1}^+ + \sigma_{Q_1}^-)$ to Q_1 with frequency $\omega_d = \omega_{12}^{Q_1}$. The first excited state splits into $|E_- \rangle$ and $|E_+ \rangle$, and the splitting separation is controlled by the Rabi frequency Ω_d . The lower spectrum $|E_- \rangle$ is treated as a new controllable excited state with modified parametric modulation. By carefully

designing the parameters, we alleviate the disturbance of $|E_+ \rangle$ to our four-band Hamiltonian.

We design the \mathbf{k} -dependent u_0 to be constant with different $k_{y,z,w}$, thus $u_0(\mathbf{k}) = f(k_x)$. With $u_{\text{max}}/2\pi = 3.46$ MHz we have $f(k_x) = \alpha(4u_{\text{max}}/\pi)(k_x + \pi)$ for $-\pi \leq k_x \leq -3\pi/4$, whereas $f(k_x) = -\alpha(4u_{\text{max}}/\pi)(k_x - \pi)$ for $-3\pi/4 \leq k_x \leq \pi$. In the range $[-3\pi/4, \pi]$, the Rabi frequency of the pump microwave field changes linearly. Figure 3(a) demonstrates that two monopoles can move along the k_x axis in the same direction with the change of A_x , while the separation remains unchanged. We set a series of different A_x , then measure the energy shift ΔE of one monopole. This shift can be considered as the response of a fictitious force $F_Y = 1$, i.e., $\Delta E = F_Y \Delta Y$ [59]. As indicated by Fig. 3(b), if we take $a = 0.5$ for example, we set $A_x = \pi/4$ and extract the eigenenergies from the spectrum data (blue), the shift of monopoles is obvious compared to $A_x = 0$ (red). For $\alpha = 1.0$, we set $A_x \in \{-2\pi/4, -\pi/4, 0, \pi/4, 2\pi/4\}$ and find the expected good linear relation between A_x and Y , the slope giving the magnetic field $B^z = -\partial_Y A_x$. We can increase the magnetic field by changing α from 1.0 to 0.25, as shown in Fig. 3(c).

C. Pseudoelectric field

It is extremely difficult to observe the topological current directly in superconducting circuits. In practice, we set the separation as a function of a fictitious time τ such that the

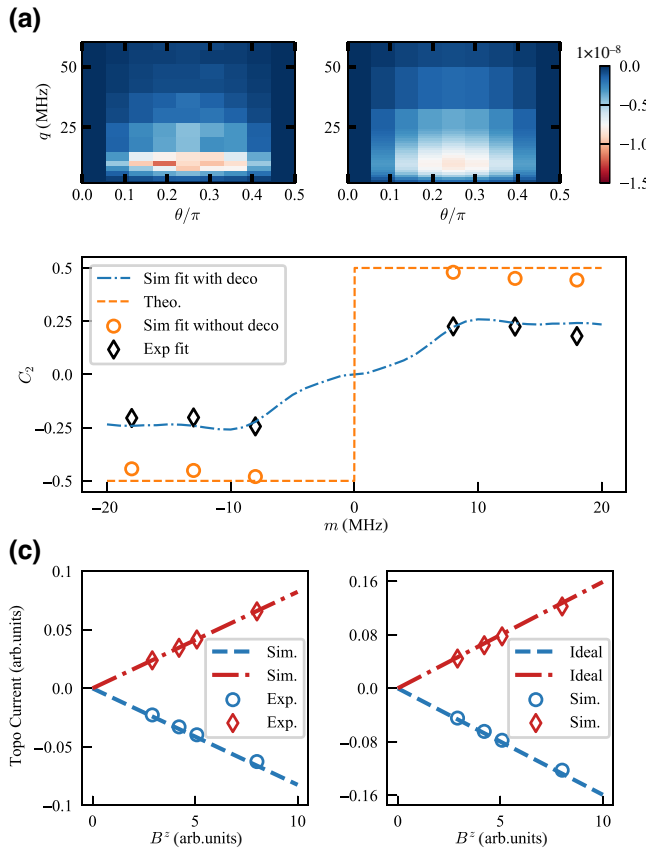


FIG. 4. SCN C_2 , Chern form $\mathcal{FF}/4\pi^2$, and current J^z . (a) Experimental (left) and simulation (right) results of Chern form $\mathcal{FF}(q, \theta)/4\pi^2$ at different q and θ . (b) The second Chern number C_2 for different m . Black symbols represent the experimental result, which agrees with the numerical simulation result after considering the decoherence, as shown by the blue dashed line. The orange dashed line is the theoretical result $C_2 = \text{sgn}(m)/2$. Orange circles show the numerical simulation without the decoherence. (c) Left panel: For different magnetic fields and modulations, experimental data and simulation results with decoherence of topological current are plotted by symbols and dashed lines. Right panel: Simulation results (symbols) without considering the decoherence align with the ideal results (dashed lines).

partial derivative of the separation concerning τ is a constant. We set $\Lambda(\tau) = \cos(0.2\pi \times \tau)$, then $\partial_\tau b_w = 0.2\pi$. The monopole separation is obtained from the spectrum measured with a fixed Λ in a discrete time τ . As shown in Fig. 3(f), with the time changing from 2 to 3 for $\alpha = 1.0$, the separation between the two monopoles varies from 0.4π to 0.6π . At the same time, we can set different α and provide different magnetic fields while modulating the monopole separation. In the first fictitious modulation, two monopoles start from $k_w = 0$ and move in opposite directions. And in the second modulation, two monopoles start from the two boundaries of the FBZ, move closer, and merge. The third modulation is almost the same as the

first, except that $\alpha = 0.5$. We show the pseudoelectric field $E_5^w = \partial_t b_w$ in Fig. 3(g).

D. Measuring the second Chern number

In this section, we show how to measure the SCN for $H_{v,+}$. For simplicity, we consider the spin-1/2 case when $a = 0$ with $C_2 = \text{sgn}(m)/2$ and label \mathbf{q}^+ as \mathbf{q} hereafter. By parametrizing \mathbf{q} into the Hopf coordinates, we obtain $q_x = q \cos \theta \cos \phi$, $q_y = q \cos \theta \sin \phi$, $q_z = q \sin \theta \cos \varphi$, and $q_w = q \sin \theta \sin \varphi$. This Dirac valley consists of two bands $E_{\pm} = \pm\sqrt{q^2 + m^2}$, each band having twofold degeneracy. In particular, we denote the lower occupied degenerate bands with eigenvalues $E_n(\mathbf{q}) = E_-$ and eigenstates $|u_n(\mathbf{q})\rangle$ where $n \in \{1, 2\}$. At this time, the SCN can be calculated in the Hopf coordinates as

$$C_2 = \frac{1}{4\pi^2} \int_{\mathbb{R}^4} \text{tr}(\mathcal{F}_{q\theta}\mathcal{F}_{\phi\varphi} + \mathcal{F}_{\varphi q}\mathcal{F}_{\phi\theta} + \mathcal{F}_{\phi q}\mathcal{F}_{\theta\varphi}) d^4q \\ = \int_0^\infty dq \int_0^{\pi/2} \mathcal{FF}(q, \theta) d\theta \int_0^{2\pi} \int_0^{2\pi} d\phi d\varphi, \quad (6)$$

where the non-Abelian Berry curvature is defined as $\mathcal{F}_{\mu\nu} = \partial_\mu \mathcal{A}_\nu - \partial_\nu \mathcal{A}_\mu - i[\mathcal{A}_\mu, \mathcal{A}_\nu]$ with the associated non-Abelian Berry connection $\mathcal{A}_\mu^{\alpha\beta} = i\langle u_\alpha | \partial_\mu | u_\beta \rangle$.

Using the analytical relations $\text{tr}(\mathcal{F}_{q\theta}\mathcal{F}_{\phi\varphi}) = \text{tr}(\mathcal{F}_{\varphi q}\mathcal{F}_{\phi\theta}) = \text{tr}(\mathcal{F}_{\phi q}\mathcal{F}_{\theta\varphi})$, we obtain $\mathcal{FF}(q, \theta) = 3mq^3 \cos \theta \sin \theta / [8\pi^2(m^2 + q^2)^{5/2}]$. Notice that $\mathcal{FF}(q, \theta)$ is independent of ϕ and φ ; without loss of generality, we set $(\phi, \varphi) = (0, 0)$ in the measurement. The Berry curvature components $\mathcal{F}_{q\theta}$ and $\mathcal{F}_{\phi\varphi}$ can be measured through the generalized geometric force in (q, θ) space. Therefore, during measurement, these quantities evolve into the tomography of each qubit with varying parameters in the 2D subspace (q, θ) . To ensure feasibility, we set a cutoff for spatial region q , i.e., $q \in [0, q_{\text{cut}}]$.

In this experiment, we measure the first-order nonadiabatic response and get the components of non-Abelian Berry curvature at $\theta \in [0, \pi/2]$ and $q \in [0, q_{\text{cut}}]$, where $q_{\text{cut}} = 200$ MHz, by slowly ramping corresponding parameters [60–64]. We use unitary transformation to increase the signal-to-noise ratio, and we apply a modified transitionless quantum driving algorithm protocol [65–69]. In Fig. 4(a), we illustrate experimental data and numerical simulation [70,71] of Berry curvature for $m = 8$ MHz. The measurement results of SCN are shown in Fig. 4(b). They can agree with the theoretical result with improved qubit coherence. In addition, with the constructed fictitious magnetic field and time-varying gapless points, we can measure the topological currents according to Eq. (5). Figure 4(c) shows the good linear relationship between topological current J^z and fictitious magnetic field B^z we simulated. Compared with the theoretical prediction, the

slope is slightly smaller, mainly caused by the short decoherence time. Ideal results can be obtained by this approach as shown in Fig. 4(c).

III. CONCLUSION AND OUTLOOK

In summary, we present the first experimental report of the quantum emulation of the PME with 4D monopoles using superconducting qubits. Additionally, we measure the fractional SCN for a 4D Dirac valley with varying mass m , indicating a topological phase transition for a 4D Dirac valley ($a = 0$) from $C_2 = -1/2$ to $C_2 = 1/2$. By treating m as the fifth dimension, it represents a five-dimensional (5D) Yang monopole [64,72] that hosts the topological charge as $Q = C_2(m > 0) - C_2(m < 0) = 1$. Notably, when $a = \pm 1$, the corresponding 5D defect gives rise to a new type of Nexus quadrupole points. This higher-dimensional generalization of the 3D Nexus triple points [73] presents an intriguing avenue for future exploration. Our work opens the possibility to explore more complex topological systems in higher dimensions using a highly tunable platform.

ACKNOWLEDGMENTS

This work was partly supported by NSFC (Grants No. 12074179, No. 11890704, and No. U21A20436), the Key R&D Program of Guangdong Province (Grant No. 2018B030326001), NSF of Jiangsu Province (Grant No. BE2021015-1), NSFC/RGC JRS (Grant No. N-HKU774/21), the CRF of Hong Kong (Grant No. C6009-20G), Innovation Program for Quantum Science and Technology (Grant No. 2021ZD0301700), and NKRDPC (Grant No. 2022YFA1405300). Work in Brussels is supported by the FRS-FNRS (Belgium), the ERC Grants TopoCold and LATIS, and the EOS project CHEQS.

APPENDIX A: PARAMETERS OF THE SUPERCONDUCTING CIRCUITS

We have measured the parameters of four qubits and couplers, shown in Table I. We also extracted the coupling parameter, $g_{QC}/2\pi \approx 100$ MHz. In the experiments, we bias all the couplers at about $\omega_c/2\pi = 6.5$ GHz; Q_1 and Q_3 are in the higher frequency band about $\omega/2\pi = 5.7$ GHz, and Q_2 and Q_4 are in the lower frequency band about $\omega/2\pi = 5.5$ GHz.

APPENDIX B: PARAMETRIC MODULATION AND PHASE CALIBRATION

Firstly, we will derive all the effective couplings between two adjacent qubits. To manipulate the interaction between two qubits (take Q_1 and Q_2 , for example) with complex coupling strength, not just the amplitude, we applied the flux bias $\phi_1(t) = \Phi_1 + \delta_1 \cos(\omega_{\phi_1} t + \varphi_1)$ to the

TABLE I. Parameters of qubits and couplers.

	Q_1	Q_2	Q_3	Q_4
$\omega/2\pi$ (GHz)	5.7254	5.5348	5.6716	5.5087
$\omega/2\pi$ (GHz) (sweet spot)	6.2383	6.4145	6.2676	6.2168
T_1 (μs)	6.83	12.17	5.05	5.12
T_ϕ (μs)	0.824	0.806	0.488	0.366
Anharmonicity (MHz)	-248.724	-254.851	-261.849	-264.020

coupler C_1 , where Φ_1 is the dc flux bias, and δ_1 , ω_{ϕ_1} , and φ_1 are the amplitude, frequency, and phase of the sinusoidal fast-flux bias modulation, respectively. When the coupler can be adiabatically eliminated, the Lamb-shifted qubit frequency is $\tilde{\omega}_{Q_{1(2)}} = \omega_{Q_{1(2)}} + [(g_{1(2),1})^2/\Delta_{1(2),1}(\phi_1)]$ and the effective coupling strength between Q_1 and Q_2 is

$$J_{12} = g_{12}^0 + \frac{g_{1,1}g_{2,1}}{2} \left(\frac{1}{\Delta_{1,1}(\phi_1)} + \frac{1}{\Delta_{2,1}(\phi_1)} \right).$$

Expanding J_{12} in the parameter $\delta_1 \cos(\omega_{\phi_1} t)$ to second order, and in the rotating frame at the qubit frequencies (including the drive-induced shift), we set the frequency of the parametric modulation at $\omega_{\phi_1} = \Delta_{12,\delta_1}$ to turn on the parametrically activated coupling and bring the excited states of qubits into resonance, where

$$\Delta_{12,\delta_1} = \tilde{\omega}_{Q_1} - \tilde{\omega}_{Q_2} + \frac{\delta_1^2}{4} \left(\frac{\partial^2 \tilde{\omega}_{Q_1}}{\partial \phi_1^2} - \frac{\partial^2 \tilde{\omega}_{Q_2}}{\partial \phi_1^2} \right).$$

Ignoring the high-order oscillation terms under the rotating-wave approximation, we get the effective Hamiltonian of the nearest two qubits:

$$\frac{H}{\hbar} = \frac{\delta_1}{2} \frac{\partial J_{12}}{\partial \phi_1} (e^{-i\varphi_1} \sigma_1^+ \sigma_2^- + e^{i\varphi_1} \sigma_1^- \sigma_2^+). \quad (\text{B1})$$

The coupling strengths in the first excited manifold can be calibrated to the same specific value by changing the parametric modulation amplitude and measuring the vacuum Rabi frequency. While the calibration of the coupling phases is less explicit, we find that the spectrum of the system with four couplings can be used to calibrate the total phase $\varphi = \varphi_1 + \varphi_2 + \varphi_3 + \varphi_4$. We assume the coupling strengths are Ω , and the Hamiltonian is

$$\frac{H}{\hbar} = \begin{bmatrix} 0 & \Omega e^{i\varphi_1} & 0 & \Omega e^{-i\varphi_4} \\ \Omega e^{-i\varphi_1} & 0 & \Omega e^{i\varphi_2} & 0 \\ 0 & \Omega e^{-i\varphi_2} & 0 & \Omega e^{i\varphi_3} \\ \Omega e^{i\varphi_4} & 0 & \Omega e^{-i\varphi_3} & 0 \end{bmatrix}. \quad (\text{B2})$$

We have $\det(H - EI) = E^4 - 4\Omega^2 E^2 + 2\Omega^4 - 2\Omega^4 \cos(\varphi) = 0$. When $\varphi = 0$, there is one doubly degenerate point. When $\varphi = \pi$, there are two doubly degenerate points. We

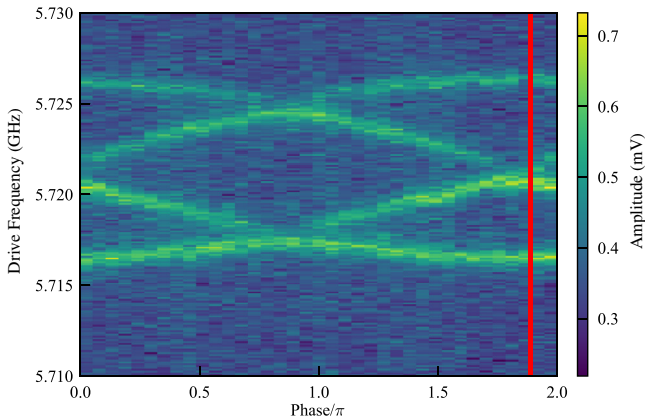


FIG. 5. Phase calibration. The energy spectrum varies with the phase of the third flux parametric modulation. The phase can be calibrated according to the number of degenerate points, as indicated by the red vertical line.

measure the spectrum varying with an arbitrary parametric modulation phase, and find that, when φ_3 shifts by $-2\pi/9$, the total phase can be well calibrated, as shown in Fig. 5.

The qubit frequency is dependent on the flux threading through the superconducting quantum interference device of couplers, $\tilde{\omega}_{Q1} = \omega_{Q1} + g_{1,1}^2/(\omega_{Q1} - \omega_{C1}(\phi))$. In parametric modulation, the effective qubit frequency is different from the static Lamb-shifted frequency. For simplicity, we can omit the second derivative of the frequency of the coupler to flux if the range of the parametric modulation is far detuned from the coupler's sweet spot and can be treated as linear. The frequency shift can be written as

$$\frac{\delta_1^2}{4} \frac{\partial^2 \tilde{\omega}_{Q1}}{\partial \phi_1^2} \approx \frac{\delta_1^2}{4} g_{1,1}^2 \frac{2}{(\omega_{Q1} - \omega_{C1})^3} \left(\frac{\partial \omega_{C1}}{\partial \phi_1} \right)^2. \quad (\text{B3})$$

So the larger the effective coupling strength, the larger the drive-induced frequency shift. It is necessary to emphasize that the average of the eigenenergies of the Hamiltonian tends to decrease on increasing the amplitude of parametric modulation. We measure the spectroscopy of the system with a constant pump field and calculate the undesired frequency shift at the same parameters for correction. We measure the spectrum with different parameters and constant $u(\mathbf{k}) = 0$, extracting the reduction of frequency as a reference, which will be compensated in later experiments and data analysis.

APPENDIX C: AUTLER-TOWNES SPLITTING

We apply a microwave with frequency $\omega_d = \omega_{12}$ and Rabi frequency Ω . There will be four dressed states in this qubit and microwave interaction system. The original first excited state $|1\rangle$ will be split into $|E_-\rangle$ and $|E_+\rangle$, whose

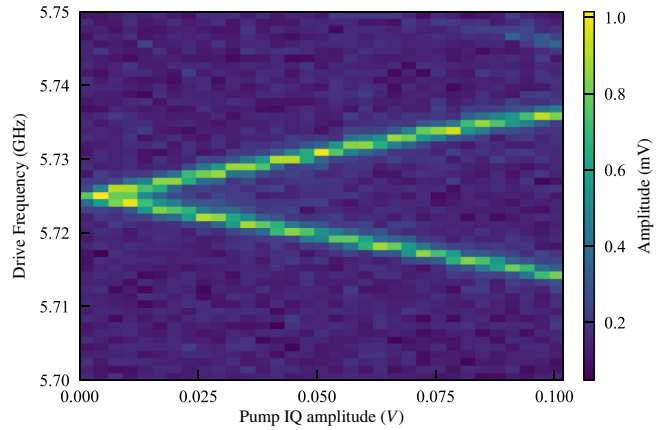


FIG. 6. Autler-Townes splitting. An additional pump microwave field splits the first excited state $|1\rangle$ into $|E_-\rangle$ and $|E_+\rangle$. The energy gap changes linearly with the amplitude of the pump IQ signal.

eigenenergies with respect to $|0\rangle$ can be written as

$$E_{\pm} = \omega_{01} + \Delta_{12}/2 \pm \sqrt{\Delta_{12}^2 + \Omega^2}/2. \quad (\text{C1})$$

We set $\Delta_{12} = 0$, the splitting equals the Rabi frequency $E_+ - E_- = \Omega$, and the frequency of $|E_-\rangle$ can be tuned easily. As illustrated in Fig. 6, we vary the amplitudes of the in-phase and quadrature (IQ) input signals and measure the spectrum. From the best fit, we find that the frequency of $|E_-\rangle$ linearly depends on the pump amplitude. The relationship between the energy shift $u_0(\mathbf{k})$ and transverse Rabi frequency $\Omega_d/2\pi$ is $u_0(\Omega_d/2\pi)/2\pi = -0.489\Omega_d/2\pi + 7.628$ MHz. In the range $[-3\pi/4, \pi]$, the Rabi frequency of the pump microwave field changed linearly from 8.536 to 15.606 MHz.

APPENDIX D: EXPERIMENTAL RESULTS FOR $a = 0$

In Fig. 7, we show the magnetic field and pseudoelectric field experimental results for $a = 0$ as a supplement to those in the main text.

APPENDIX E: MEASUREMENT OF THE SECOND CHERN NUMBER

In the Hopf coordinates, when $(\phi, \varphi) = (0, 0)$, $H_{v,\pm}$ is $H_{\phi=\varphi=0} = q \cos \theta \tilde{\Gamma}_x + q \sin \theta \tilde{\Gamma}_z + m \tilde{\Gamma}_0$. In order to reduce the inaccuracy in preparation of the initial state, we rotate the Hamiltonian so that we just need to prepare the same eigenstates at different parameters with the following unitary diagonalization:

$$H_{\text{rot}} = U H_{\phi=\varphi=0} U^\dagger, \quad (\text{E1})$$

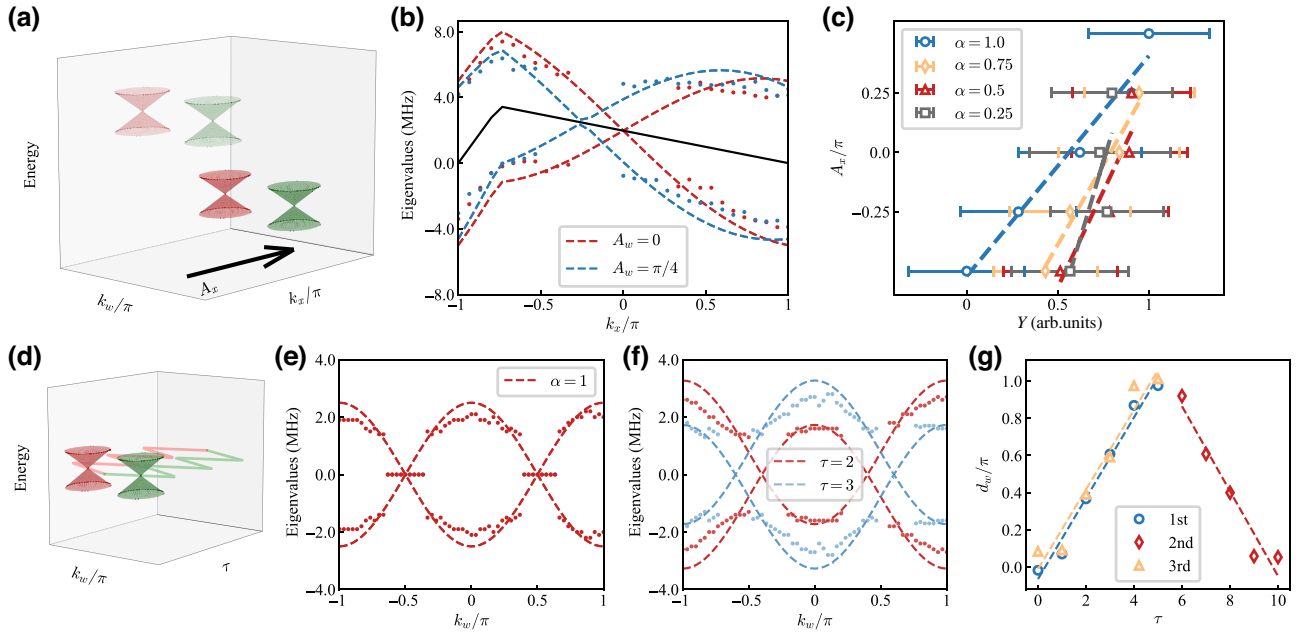


FIG. 7. Experimental results for $a = 0$. (a)–(c) The construction of magnetic field B^z . (d)–(g) The modulation of separation of spin-1/2 monopole, which can be considered as a pseudoelectric field.

where $U = U_1 U_2$ and $\Phi = \arccos(m/\sqrt{q^2 + m^2})$ with

$$U_1 = \begin{bmatrix} \cos(\Phi/2) & \sin(\Phi/2) & 0 & 0 \\ -\sin(\Phi/2) & \cos(\Phi/2) & 0 & 0 \\ 0 & 0 & \cos(\Phi/2) & -\sin(\Phi/2) \\ 0 & 0 & \sin(\Phi/2) & \cos(\Phi/2) \end{bmatrix}, \quad (\text{E2})$$

$$U_2 = \begin{bmatrix} e^{i\theta/2} & 0 & 0 & 0 \\ 0 & e^{-i\theta/2} & 0 & 0 \\ 0 & 0 & e^{i\theta/2} & 0 \\ 0 & 0 & 0 & e^{-i\theta/2} \end{bmatrix}. \quad (\text{E3})$$

In this experiment, we measure the nonadiabatic response to obtain the Berry curvature [63]. In this protocol, we slowly ramp the parameter $\mu(t)$ of the quantum system initialized at $|\Psi_i\rangle$, with a speed v , yielding that the generalized geometric force $M_v = -\langle \partial_v H \rangle$ with the relation $M_v = -\dot{\mu} \langle \mathcal{F}_{\mu v}^{ii} \rangle + \text{const}$. By ramping $\mu(t)$ with the speed $v/2$, we obtain the Berry curvature $\mathcal{F}_{\mu v}^{ii} \approx 2[M_v(v/2) - M_v(v)]/v$. This procedure is executed with four initial states $|\Psi_1\rangle = |\Psi_A\rangle$, $|\Psi_2\rangle = |\Psi_B\rangle$, $|\Psi_3\rangle = (|\Psi_A\rangle + |\Psi_B\rangle)/\sqrt{2}$, and $|\Psi_4\rangle = (|\Psi_A\rangle + i|\Psi_B\rangle)/\sqrt{2}$, where $|\Psi_A\rangle$ and $|\Psi_B\rangle$ are eigenstates of H_{rot} . Then we get the non-Abelian Berry curvature as

$$\mathcal{F}_{\mu v} = \begin{bmatrix} \mathcal{F}_{\mu v}^{AA} & \mathcal{F}_{\mu v}^{AB} \\ (\mathcal{F}_{\mu v}^{AB})^* & \mathcal{F}_{\mu v}^{BB} \end{bmatrix}, \quad (\text{E4})$$

where $\mathcal{F}_{\mu v}^{AA} = \mathcal{F}_{\mu v}^{11}$, $\mathcal{F}_{\mu v}^{BB} = \mathcal{F}_{\mu v}^{22}$, and $\mathcal{F}_{\mu v}^{AB} = 2i\mathcal{F}_{\mu v}^{33} + 2\mathcal{F}_{\mu v}^{44} - (1+i)(\mathcal{F}_{\mu v}^{11} + \mathcal{F}_{\mu v}^{22})$.

In this experiment, we first ramp $q(t) = q_0 + v_1(t - t_m)t^2/t_m^2$ and measure $M_\theta = q \sin \theta \tilde{\Gamma}_x - q \cos \theta \tilde{\Gamma}_z$ to obtain $\mathcal{F}_{q\theta}$, as shown in Fig. 8. Similarly, $\mathcal{F}_{\phi\phi}$ is obtained by measuring $M_\phi = -q \sin \theta \tilde{\Gamma}_w$ with ramping $\phi(t) = \phi_0 + v_2(t - t_m)t^2/t_m^2$. For different m , we choose different but efficient q values to depict the profile. For every θ , we fit $\mathcal{F}(q, \theta)$ which varies with q according to the analytical result, and choose $q_{\text{cut}} = 200$ MHz in the numerical integration, as shown in Fig. 9. The expectation value can be quite small on account of the small perturbation term.

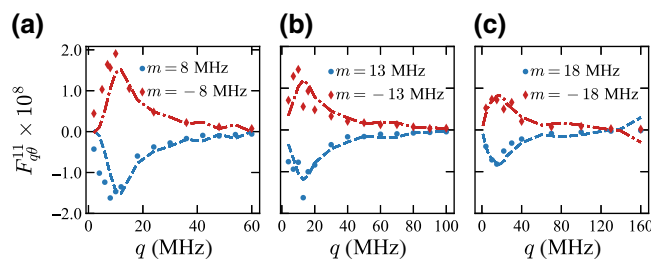


FIG. 8. According to the measurement of geometric force, calculated results of $\mathcal{F}_{q\theta}^{11}$ are illustrated for (a) $m = \pm 8$ MHz, (b) $m = \pm 13$ MHz, and (c) $m = \pm 18$ MHz. The symbols are experimental results and the dashed lines are numerical simulations considering the decoherence.

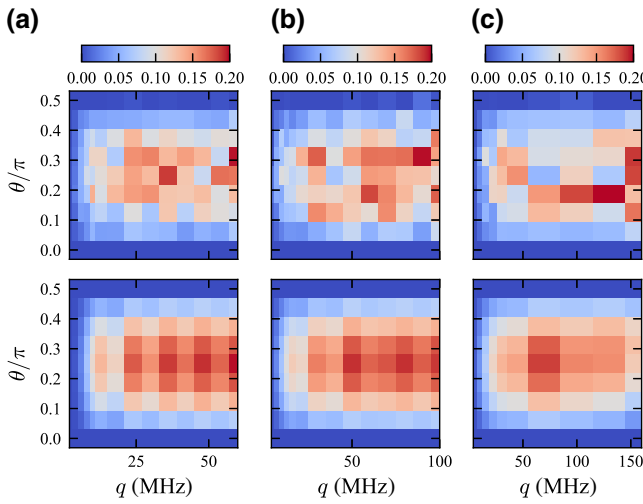


FIG. 9. Calculated results of $\mathcal{F}_{\phi\phi}^{11}$ under the second kind of ramp for (a) $m = 8$ MHz, (b) $m = 13$ MHz, and (c) $m = 18$ MHz. For each column, the upper panel is the experimental data, and the lower panel is the numerical simulation considering the decoherence.

Precise measurement of the nonadiabatic response is a difficult task for practical implementation. We use the modified transitionless quantum driving algorithm (TQDA) protocol to increase the measurement signal-to-noise ratio. In the original routine, the counterdiabatic term $H_{CD} = i \sum |n\rangle \langle n|$ is introduced to cancel the perturbation in the adiabatic process, where $|n\rangle$ is an eigenstate of H_0 . In our protocol, we design the Hamiltonian as $H = H_0 + \lambda H_{CD}$, where λ is named as the TQDA factor. We can increase the nonadiabatic response in an appropriate range, while the generalized geometric force M_v varies linearly with λ . In practice, we set a suitable list of TQDA factors for different parameters, as shown in Fig. 10.

After the modified ramping evolution, we measure $M_v(\lambda)$. The observable could be amplified sufficiently

and then we fit the slope k of $M_v(\lambda)$, and extract the nonadiabatic response $M_v(\lambda = 0) = -k$:

$$H_{\text{ramp1}}^{\text{CD}} = \frac{\lambda}{2} \frac{m}{q^2(t) + m^2} \dot{q}(t) \sigma_y, \quad (\text{E5})$$

$$H_{\text{ramp2}}^{\text{CD}} = \frac{-\lambda}{2} \frac{\sqrt{q^2 + m^2} q \cos \theta \cos \phi(t)}{q^2 + m^2 + [q \cos \theta \sin \phi(t)]^2} \dot{\phi}(t) \sigma_x. \quad (\text{E6})$$

After the transformation, we just need to measure

$$M_\theta^{\text{rot}} = U M_\theta U^\dagger \begin{bmatrix} 0 & iq & 0 & 0 \\ -iq & 0 & 0 & 0 \\ 0 & 0 & 0 & iq \\ 0 & 0 & -iq & 0 \end{bmatrix}, \quad (\text{E7})$$

$$M_\varphi^{\text{rot}} = U M_\varphi U^\dagger \begin{bmatrix} 0 & 0 & -q \sin \theta & 0 \\ 0 & 0 & 0 & q \sin \theta \\ -q \sin \theta & 0 & 0 & 0 \\ 0 & q \sin \theta & 0 & 0 \end{bmatrix}. \quad (\text{E8})$$

APPENDIX F: FRACTIONAL SECOND CHERN NUMBER FOR THE GAPPED DIRAC VALLEYS

After introducing a mass term into the 4D gapless model, we obtain a fully gapped insulator with the total Hamiltonian $H_v = H(\mathbf{k}) + \tilde{m}$, which hosts two Dirac-like valleys along the k_w direction, as shown in Fig. 11. The valley Hamiltonian near \mathbf{K}_+ (\mathbf{K}_-) is given by

$$H_{v,\pm} = q_x \tilde{\Gamma}_x + q_x \tilde{\Gamma}_x + q_z \tilde{\Gamma}_z \pm q_w \tilde{\Gamma}_w + m \tilde{\Gamma}_0. \quad (\text{F1})$$

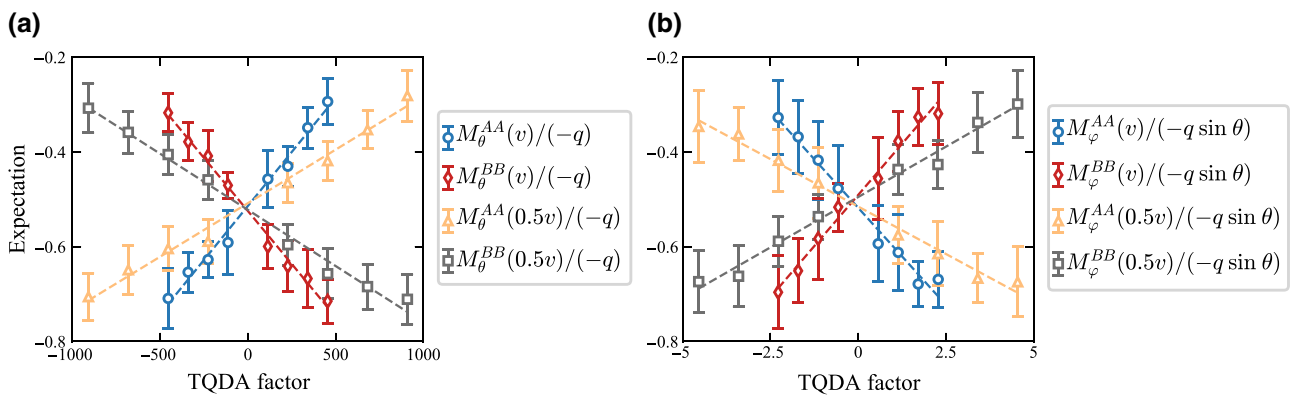


FIG. 10. TQDA. (a) The first ramp at $q = 54$ MHz. We measure the results for different initial states and ramping speeds. Expectation values change linearly with the TQDA factor. The circles represent experimental data and the dashed lines are the best fits. (b) The second ramp at $q = 6$ MHz and $\theta = 0$.

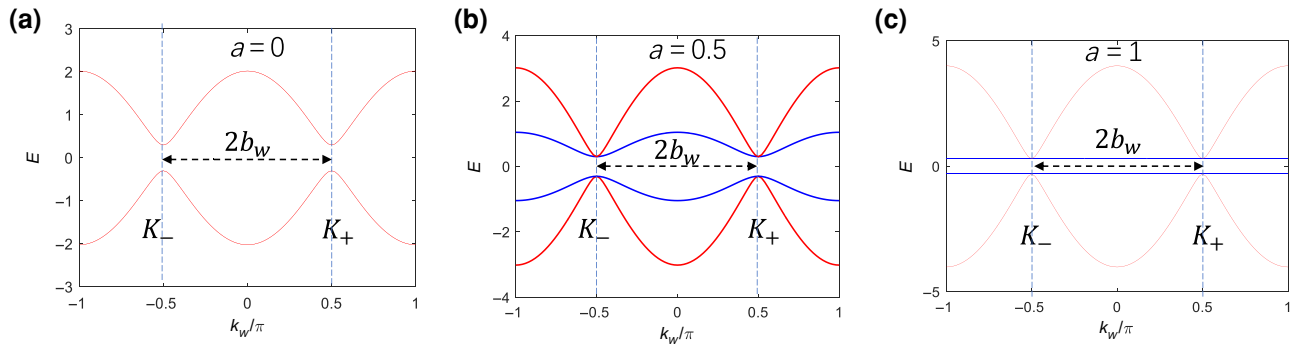


FIG. 11. Schematic of the spectrum of the gapped lattice model $H_v = H(\mathbf{k}) + \tilde{m}$ when (a) $a = 0$, (b) $a = 0.5$, and (c) $a = 1$.

Each valley hosts the second Chern number

$$\begin{aligned} C_2^\pm &= \frac{1}{32\pi^2} \int_{\mathbb{R}^4} d^4q \epsilon^{\mu\nu\alpha\beta} \text{tr}(\mathcal{F}_{\mu\nu}^\pm \mathcal{F}_{\alpha\beta}^\pm) \\ &= \frac{1}{4\pi^2} \int_{\mathbb{R}^4} d^4q \text{tr}(\mathcal{F}_{xy}^\pm \mathcal{F}_{zw}^\pm + \mathcal{F}_{wx}^\pm \mathcal{F}_{zy}^\pm + \mathcal{F}_{zx}^\pm \mathcal{F}_{yw}^\pm) \\ &= \begin{cases} \pm \text{sgn}(m)/2, & a \neq \pm 1, \\ \pm \text{sgn}(m)/8, & a = 1, \end{cases} \end{aligned} \quad (\text{F2})$$

for $a \geq 0$. Here \mathbb{R}^4 denotes the full 4D real space; and $\mathcal{F}_{\mu\nu}^\pm$ denotes the non-Abelian Berry curvature defined for the lower two occupied bands of each valley at \mathbf{K}_+ and \mathbf{K}_- , respectively. In fact, these two valleys host opposite second Chern numbers, leading to a total zero second Chern number $C_2 = C_2^+ + C_2^- = 0$ for this phase. One could define a valley second Chern number for this model, i.e., $C_{2,v} = (C_2^+ - C_2^-)/2$.

APPENDIX G: THE 5D YANG MONOPOLE AND NEXUS QUADRUPOLE NODAL POINTS

By treating m as the fifth dimension q_u , we obtain a 5D model for a single nodal point. Its Hamiltonian takes the

form

$$H_{5D}(\mathbf{q}) = q_x \tilde{\Gamma}_x + q_y \tilde{\Gamma}_y + q_z \tilde{\Gamma}_z + q_w \tilde{\Gamma}_w + q_u \tilde{\Gamma}_0, \quad (\text{G1})$$

where the energy spectrum

$$E = \pm \sqrt{(1 \pm a)^2 (q_x^2 + q_y^2 + q_z^2 + q_w^2) + q_u^2}. \quad (\text{G2})$$

When $a = 0$, this is a standard 5D Yang monopole [64] in momentum space whose topological charge is given by

$$\begin{aligned} Q &= C_2 = \frac{1}{32\pi^2} \int_{\mathbb{S}^4} \text{tr}(\mathcal{F}_{\mu\nu} \mathcal{F}_{\alpha\beta}) d^4q \\ &= C_2(q_u > 0) - C_2(q_u < 0) = 1. \end{aligned} \quad (\text{G3})$$

In this case there is a full gap between the lower occupied and the higher empty bands except $q = 0$. Thus we can calculate the second Chern number for the lower twofold-degenerate bands on the hypersphere \mathbb{S}^4 enclosing the monopole. The monopole charge actually is equivalent to the difference between two massive 4D Dirac valleys when taking q_u as a constant. For $|a| > 0$ and $|a| \neq 1$, there is still a full gap between the lower occupied and the higher

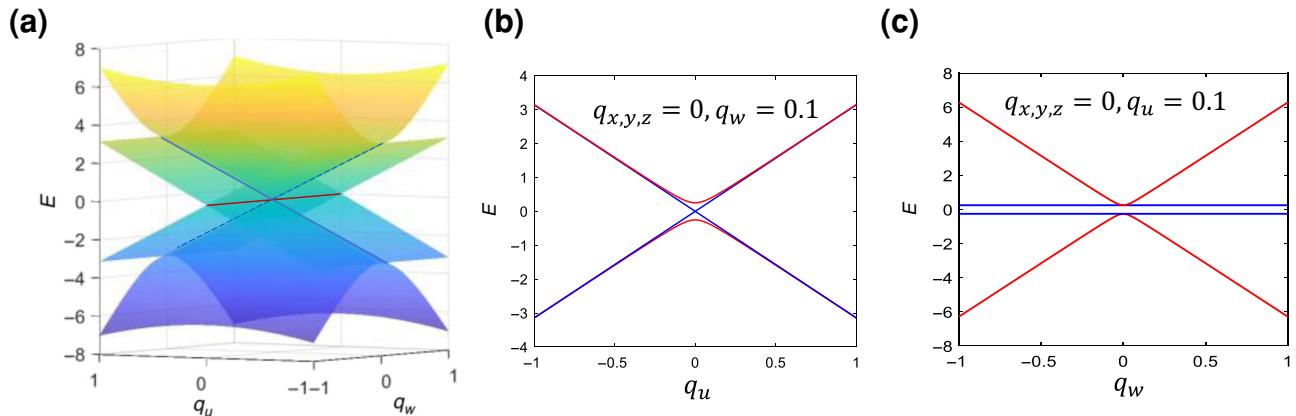


FIG. 12. The 5D Nexus fermion H_{5D} when $a = 1$. (a) Schematic of the spectrum when $q_x = q_y = q_z = 0$. (b),(c) Slices for E when (b) $q_w = 0.1$ and (c) $q_u = 0.1$.

empty bands beyond the defect. The situation is similar to the case when $a = 0$, which hosts a charge $Q = 1$.

However, when $|a| = 1$, the spectrum becomes

$$E = \pm q_u \pm \sqrt{4(q_x^2 + q_y^2 + q_z^2 + q_w^2) + q_u^2}. \quad (\text{G4})$$

As shown in Fig. 12, this is not a nodal point defect any more. One could not introduce a \mathbb{S}^4 to fully enclose this defect with a total gapped spectrum on this surface. This is a new type of Nexus fermion with fourfold degeneracy along the nodal line. The topological punctured Chern invariant should be generalized from the 3D Nexus triple points [73] on the corresponding punctured manifold in the future.

- [1] M. Z. Hasan and C. L. Kane, Colloquium: Topological insulators, *Rev. Mod. Phys.* **82**, 3045 (2010).
- [2] X.-L. Qi and S.-C. Zhang, Topological insulators and superconductors, *Rev. Mod. Phys.* **83**, 1057 (2011).
- [3] N. P. Armitage, E. J. Mele, and A. Vishwanath, Weyl and Dirac semimetals in three-dimensional solids, *Rev. Mod. Phys.* **90**, 015001 (2018).
- [4] D.-W. Zhang, Y.-Q. Zhu, Y. X. Zhao, H. Yan, and S.-L. Zhu, Topological quantum matter with cold atoms, *Adv. Phys.* **67**, 253 (2018).
- [5] N. R. Cooper, J. Dalibard, and I. B. Spielman, Topological bands for ultracold atoms, *Rev. Mod. Phys.* **91**, 015005 (2019).
- [6] Y. Xu, Topological gapless matters in three-dimensional ultracold atomic gases, *Front. Phys.* **14**, e1d 43402 (2019).
- [7] T. Ozawa, *et al.*, Topological photonics, *Rev. Mod. Phys.* **91**, 015006 (2019).
- [8] W. Zhu, W. Deng, Y. Liu, J. Lu, Z.-K. Lin, H.-X. Wang, X. Huang, J.-H. Jiang, and Z. Liu, Topological phononic metamaterials, *ArXiv:2303.01426* (2023).
- [9] R.-P. Riwar, M. Houzet, J. S. Meyer, and Y. V. Nazarov, Multi-terminal Josephson junctions as topological matter, *Nat. Commun.* **7**, 11167 (2016).
- [10] R. A. Bertlmann, *Anomalies in Quantum Field Theory* (Oxford University Press, New York, 2000).
- [11] E. Fradkin, *Field Theories of Condensed Matter Physics* (Cambridge University Press, New York, 2013), 2nd ed.
- [12] A. A. Zyuzin and A. A. Burkov, Topological response in Weyl semimetals and the chiral anomaly, *Phys. Rev. B* **86**, 115133 (2012).
- [13] M. M. Vazifeh and M. Franz, Electromagnetic Response of Weyl Semimetals, *Phys. Rev. Lett.* **111**, 027201 (2013).
- [14] D. I. Pikulin, A. Chen, and M. Franz, Chiral Anomaly from Strain-Induced Gauge Fields in Dirac and Weyl Semimetals, *Phys. Rev. X* **6**, 041021 (2016).
- [15] J. Behrends, S. Roy, M. H. Kolodrubetz, J. H. Bardarson, and A. G. Grushin, Landau levels, Bardeen polynomials, and Fermi arcs in Weyl semimetals: Lattice-based approach to the chiral anomaly, *Phys. Rev. B* **99**, 140201(R) (2019).
- [16] Z. Zheng, Z. Lin, D.-W. Zhang, S.-L. Zhu, and Z. D. Wang, Chiral magnetic effect in three-dimensional optical lattices, *Phys. Rev. Res.* **1**, 033102 (2019).
- [17] Z. Lin, X.-J. Huang, D.-W. Zhang, S.-L. Zhu, and Z. D. Wang, Emulating topological currents arising from a dipolar parity anomaly in two-dimensional optical lattices, *Phys. Rev. A* **99**, 043419 (2019).
- [18] H. Shapourian, T. L. Hughes, and S. Ryu, Viscoelastic response of topological tight-binding models in two and three dimensions, *Phys. Rev. B* **92**, 165131 (2015).
- [19] A. Cortijo, Y. Ferreira, K. Landsteiner, and M. A. H. Vozmediano, Elastic Gauge Fields in Weyl Semimetals, *Phys. Rev. Lett.* **115**, 177202 (2015).
- [20] A. G. Grushin, J. W. F. Venderbos, A. Vishwanath, and R. Ilan, Inhomogeneous Weyl and Dirac Semimetals: Transport in Axial Magnetic Fields and Fermi Arc Surface States from Pseudo-Landau Levels, *Phys. Rev. X* **6**, 041046 (2016).
- [21] X.-L. Qi, T. L. Hughes, and S.-C. Zhang, Topological field theory of time-reversal invariant insulators, *Phys. Rev. B* **78**, 195424 (2008).
- [22] S.-C. Zhang and J. Hu, A four-dimensional generalization of the quantum Hall effect, *Science* **294**, 823 (2001).
- [23] D. Karabali and V. Nair, Quantum Hall effect in higher dimensions, *Nucl. Phys. B* **641**, 533 (2002).
- [24] H. Price, O. Zilberberg, T. Ozawa, I. Carusotto, and N. Goldman, Four-Dimensional Quantum Hall Effect with Ultracold Atoms, *Phys. Rev. Lett.* **115**, 195303 (2015).
- [25] Y. E. Kraus, Z. Ringel, and O. Zilberberg, Four-Dimensional Quantum Hall Effect in a Two-Dimensional Quasicrystal, *Phys. Rev. Lett.* **111**, 226401 (2013).
- [26] M. Lohse, C. Schweizer, H. M. Price, O. Zilberberg, and I. Bloch, Exploring 4D quantum Hall physics with a 2D topological charge pump, *Nature* **553**, 55 (2018).
- [27] J.-B. Bouhiron, A. Fabre, Q. Liu, Q. Redon, N. Mittal, T. Satoor, R. Lopes, and S. Nascimbene, Realization of an atomic quantum Hall system in four dimensions, *ArXiv:2210.06322* (2022).
- [28] O. Zilberberg, S. Huang, J. Guglielmon, M. Wang, K. P. Chen, Y. E. Kraus, and M. C. Rechtsman, Photonic topological boundary pumping as a probe of 4D quantum Hall physics, *Nature* **553**, 59 (2018).
- [29] G. Palumbo and N. Goldman, Revealing Tensor Monopoles through Quantum-Metric Measurements, *Phys. Rev. Lett.* **121**, 170401 (2018).
- [30] G. Palumbo and N. Goldman, Tensor Berry connections and their topological invariants, *Phys. Rev. B* **99**, 045154 (2019).
- [31] Y.-Q. Zhu, N. Goldman, and G. Palumbo, Four-dimensional semimetals with tensor monopoles: From surface states to topological responses, *Phys. Rev. B* **102**, 081109(R) (2020).
- [32] H. Weisbrich, M. Bestler, and W. Belzig, Tensor Monopoles in superconducting systems, *Quantum* **5**, 601 (2021).
- [33] H.-T. Ding, Y.-Q. Zhu, Z. Li, and L. Shao, Tensor monopoles and the negative magnetoresistance effect in optical lattices, *Phys. Rev. A* **102**, 053325 (2020).
- [34] X. Tan, *et al.*, Experimental Observation of Tensor Monopoles with a Superconducting Qudit, *Phys. Rev. Lett.* **126**, 017702 (2021).
- [35] M. Chen, C. Li, G. Palumbo, Y.-Q. Zhu, N. Goldman, and P. Cappellaro, A synthetic monopole source of Kalb-Ramond field in diamond, *Science* **375**, 1017 (2022).

- [36] Y.-Q. Zhu, Z. Zheng, G. Palumbo, and Z. D. Wang, Topological Electromagnetic Effects and Higher Second Chern Numbers in Four-Dimensional Gapped Phases, *Phys. Rev. Lett.* **129**, 196602 (2022).
- [37] J. Koch, T. M. Yu, J. Gambetta, A. A. Houck, D. I. Schuster, J. Majer, A. Blais, M. H. Devoret, S. M. Girvin, and R. J. Schoelkopf, Charge-insensitive qubit design derived from the Cooper pair box, *Phys. Rev. A* **76**, 042319 (2007).
- [38] R. Barends, *et al.*, Coherent Josephson Qubit Suitable for Scalable Quantum Integrated Circuits, *Phys. Rev. Lett.* **111**, 080502 (2013).
- [39] J.-Q. You and F. Nori, Atomic physics and quantum optics using superconducting circuits, *Nature* **474**, 589 (2011).
- [40] F. Arute, *et al.*, Quantum supremacy using a programmable superconducting processor, *Nature* **574**, 505 (2019).
- [41] Y. Wu, *et al.*, Strong Quantum Computational Advantage Using a Superconducting Quantum Processor, *Phys. Rev. Lett.* **127**, 180501 (2021).
- [42] P. Zhao, K. Linghu, Z. Li, P. Xu, R. Wang, G. Xue, Y. Jin, and H. Yu, Quantum Crosstalk Analysis for Simultaneous Gate Operations on Superconducting Qubits, *PRX Quantum* **3**, 020301 (2022).
- [43] D. M. Zajac, *et al.*, Spectator errors in tunable coupling architectures, *ArXiv:2108.11221* (2021).
- [44] J. Chu and F. Yan, Coupler-assisted controlled-phase gate with enhanced adiabaticity, *Phys. Rev. Appl.* **16**, 054020 (2021).
- [45] F. Yan, P. Krantz, Y. Sung, M. Kjaergaard, D. L. Campbell, T. P. Orlando, S. Gustavsson, and W. D. Oliver, Tunable coupling scheme for implementing high-fidelity two-qubit gates, *Phys. Rev. Appl.* **10**, 054062 (2018).
- [46] E. A. Sete, A. Q. Chen, R. Manenti, S. Kulshreshtha, and S. Poletto, Floating tunable coupler for scalable quantum computing architectures, *Phys. Rev. Appl.* **15**, 064063 (2021).
- [47] J. Stehlík, *et al.*, Tunable Coupling Architecture for Fixed-Frequency Transmon Superconducting Qubits, *Phys. Rev. Lett.* **127**, 080505 (2021).
- [48] D. C. McKay, S. Filipp, A. Mezzacapo, E. Magesan, J. M. Chow, and J. M. Gambetta, Universal gate for fixed-frequency qubits via a tunable bus, *Phys. Rev. Appl.* **6**, 064007 (2016).
- [49] M. Roth, M. Ganzhorn, N. Moll, S. Filipp, G. Salis, and S. Schmidt, Analysis of a parametrically driven exchange-type gate and a two-photon excitation gate between superconducting qubits, *Phys. Rev. A* **96**, 062323 (2017).
- [50] M. Reagor, *et al.*, Demonstration of universal parametric entangling gates on a multi-qubit lattice, *Sci. Adv.* **4**, eaao3603 (2018).
- [51] M. Ganzhorn, *et al.*, Gate-efficient simulation of molecular eigenstates on a quantum computer, *Phys. Rev. Appl.* **11**, 044092 (2019).
- [52] P. Mundada, G. Zhang, T. Hazard, and A. Houck, Suppression of qubit crosstalk in a tunable coupling superconducting circuit, *Phys. Rev. Appl.* **12**, 054023 (2019).
- [53] M. Ganzhorn, *et al.*, Benchmarking the noise sensitivity of different parametric two-qubit gates in a single superconducting quantum computing platform, *Phys. Rev. Res.* **2**, 033447 (2020).
- [54] S. Roy, M. Kolodrubetz, N. Goldman, and A. G. Grushin, Tunable axial gauge fields in engineered Weyl semimetals: Semiclassical analysis and optical lattice implementations, *2D Mater.* **5**, 024001 (2018).
- [55] B. R. Mollow, Power spectrum of light scattered by two-level systems, *Phys. Rev.* **188**, 1969 (1969).
- [56] M. Baur, S. Filipp, R. Bianchetti, J. M. Fink, M. Göppel, L. Steffen, P. J. Leek, A. Blais, and A. Wallraff, Measurement of Autler-Townes and Mollow Transitions in a Strongly Driven Superconducting Qubit, *Phys. Rev. Lett.* **102**, 243602 (2009).
- [57] M. A. Sillanpää, J. Li, K. Cicak, F. Altomare, J. I. Park, R. W. Simmonds, G. S. Paraoanu, and P. J. Hakonen, Autler-Townes Effect in a Superconducting Three-Level System, *Phys. Rev. Lett.* **103**, 193601 (2009).
- [58] H.-C. Sun, Y.-x. Liu, H. Ian, J. Q. You, E. Il'ichev, and F. Nori, Electromagnetically induced transparency and Autler-Townes splitting in superconducting flux quantum circuits, *Phys. Rev. A* **89**, 063822 (2014).
- [59] X. Tan, Y. X. Zhao, Q. Liu, G. Xue, H.-F. Yu, Z. D. Wang, and Y. Yu, Simulation and Manipulation of Tunable Weyl-Semimetal Bands Using Superconducting Quantum Circuits, *Phys. Rev. Lett.* **122**, 010501 (2019).
- [60] V. Gritsev and A. Polkovnikov, Dynamical quantum Hall effect in the parameter space, *Proc. Natl. Acad. Sci. U.S.A.* **109**, 6457 (2012).
- [61] M. D. Schroer, M. H. Kolodrubetz, W. F. Kindel, M. Sandberg, J. Gao, M. R. Vissers, D. P. Pappas, A. Polkovnikov, and K. W. Lehnert, Measuring a Topological Transition in an Artificial Spin-1/2 System, *Phys. Rev. Lett.* **113**, 050402 (2014).
- [62] P. Roushan, *et al.*, Observation of topological transitions in interacting quantum circuits, *Nature* **515**, 241 (2014).
- [63] M. Kolodrubetz, Measuring the Second Chern Number from Nonadiabatic Effects, *Phys. Rev. Lett.* **117**, 015301 (2016).
- [64] S. Sugawa, F. Salces-Carcoba, A. R. Perry, Y. Yue, and I. B. Spielman, Second Chern number of a quantum-simulated non-Abelian Yang monopole, *Science* **360**, 1429 (2018).
- [65] M. V. Berry, Transitionless quantum driving, *J. Phys. A: Math. Theor.* **42**, 365303 (2009).
- [66] M. Demirplak and S. A. Rice, On the consistency, extremal, and global properties of counterdiabatic fields, *J. Chem. Phys.* **129**, 154111 (2008).
- [67] A. del Campo, Shortcuts to Adiabaticity by Counterdiabatic Driving, *Phys. Rev. Lett.* **111**, 100502 (2013).
- [68] R. Unanyan, L. Yatsenko, K. Bergmann, and B. Shore, Laser-induced adiabatic atomic reorientation with control of diabatic losses, *Opt. Commun.* **139**, 48 (1997).
- [69] X. Chen, I. Lizuain, A. Ruschhaupt, D. Guéry-Odelin, and J. G. Muga, Shortcut to Adiabatic Passage in Two- and Three-Level Atoms, *Phys. Rev. Lett.* **105**, 123003 (2010).
- [70] J. Johansson, P. Nation, and F. Nori, QuTiP: An open-source Python framework for the dynamics of open quantum systems, *Comput. Phys. Commun.* **183**, 1760 (2012).
- [71] J. Johansson, P. Nation, and F. Nori, QuTiP 2: A Python framework for the dynamics of open quantum systems, *Comput. Phys. Commun.* **184**, 1234 (2013).
- [72] C. N. Yang, Generalization of Dirac's monopole to SU2 gauge fields, *J. Math. Phys.* **19**, 320 (1978).
- [73] A. Das, E. Cornfeld, and S. Pujari, Punctured-Chern Topological Invariants for Semimetallic Band Structures, *Phys. Rev. Lett.* **130**, 186202 (2023).